Study of LiCoO₂/Li₇La₃Zr₂O₁₂:Ta Interface

Degradation in All-Solid-State Lithium Battery

Martin Ihrig^{*a,b}, Martin Finsterbusch^{*a,c,d}, Alexander M. Laptev^a, Chia-hao Tu^e, Ngoc Thanh
Thuy Tran^e, Che-an Lin^f, Liang-Yin Kuo^a, Ruijie Ye^a, Yoo Jung Sohn^a, Payam Kaghazchi^a, Shih-kang Lin^{e,f,g}, Dina Fattakhova-Rohlfing^{*a,c,h}, and Olivier Guillon^{a,b,c,d}

^a Institute of Energy and Climate Research – Materials Synthesis and Processing, Forschungszentrum Jülich GmbH, 52425 Jülich, Germany

^b Institute of Mineral Engineering, RWTH Aachen University, Mauerstr. 5, 52064 Aachen, Germany

^c Jülich-Aachen Research Alliance: JARA-ENERGY, 52425 Jülich, Germany

^d Helmholtz Institute Münster: Ionics in Energy Storage, Corrensstr. 46, 48149 Münster, Germany

^e Hierarchical Green-Energy Materials Research Center, National Cheng Kung University, No.1, University Rd., Tainan City 701, Taiwan

^f Department of Materials Science and Engineering, National Cheng Kung University, No.1, University Rd., Tainan City 701, Taiwan

g Program on Smart and Sustainable Manufacturing, Academy of Innovative Semiconductor and Sustainable Manufacturing, National Cheng Kung University, No.1, University Rd., Tainan City 701, Taiwan

^h Faculty of Engineering and Center for Nanointegration Duisburg-Essen, University of Duisburg-Essen, Lotharstr. 1, 47057 Duisburg, Germany

KEYWORDS: ASSLB, LCO/LLZO:Ta interface, interface degradation, Al diffusion, Co diffusion, electrochemical impedance spectroscopy

ABSTRACT: The garnet-type Li₇La₃Zr₂O₁₂ (LLZO) ceramic solid electrolyte combines high Liion conductivity at room temperature with high chemical stability. Several all-solid-state Li batteries featuring the LLZO electrolyte and the LiCoO₂ (LCO) or LiCoO₂-LLZO composite cathode were demonstrated. However, all batteries exhibit rapid capacity fading during cycling, which is often attributed to the formation of cracks due to volume expansion and the contraction of LCO. Excluding the possibility of mechanical failure due to crack formation between the LiCoO₂/LLZO interface, a detailed investigation of the LiCoO₂/LLZO interface before and after cycling clearly demonstrated cation diffusion between the LiCoO₂ and the LLZO. This electrochemically driven cation diffusion during cycling causes the formation of an amorphous secondary phase interlayer with high impedance, leading to the observed capacity fading. Furthermore, thermodynamic analysis using density functional theory confirms the possibility of low- or non-conducting secondary phases forming during cycling and offers an additional explanation for the observed capacity fading. Understanding the presented degradation paves the way to increasing the cycling stability of ceramic all-solid-state Li batteries.

1. INTRODUCTION

All-solid-state Li batteries (ASSLBs) are a promising solution to overcome the limitations of conventional Li-ion batteries such as low temperature stability, limited safety, and modest energy storage capacity. Among the ceramic-based solid electrolytes, 5,5-10 the Li₇La₃Zr₂O₁₂ (LLZO) garnet has attracted the attention of researchers and engineers. LLZO exhibits high Li-ion conductivity (increased via doping by Al and Ta), a broad electrochemical window, and stability against lithium. Significant progress has been achieved in the development and operation of Li batteries with a LLZO electrolyte, a LiCoO₂ (LCO) cathode, and a Li anode. Nevertheless, the fabrication of reliable LCO|LLZO half-cells remains a challenging task. Moreover, little is known about the properties of the LCO/LLZO interface upon processing and operation, including the development of its microstructure, phase composition, and charge transfer. Moreover.

A high sintering temperature is typically needed to achieve the required mechanical stability and Li-ion conductivity of LLZO-based half-cells.¹⁸⁻¹⁹ However, long-term exposure to elevated temperature with conventional free sintering causes atomic interdiffusion with the formation of secondary phases.^{20–23} The formation of these secondary phases results in the enhanced impedance of LLZO-based ASSLBs. Thus, a high sintering temperature and a long free sintering time is an essential obstacle to the fabrication of durable ceramic Li batteries.^{1, 3} LCO|LLZO half-cells with a relatively low impedance can be successfully fabricated at low sintering temperatures and without sintering additives using the pressure-supported field-assisted sintering technique, also known as spark plasma sintering (FAST/SPS).²⁴⁻²⁵ The interfacial reactions during FAST/SPS can be suppressed or significantly diminished due to the short processing time and the reduced sintering temperature.

The literature offers several examples of LCO|LLZO-based batteries.^{1, 3} However, a drawback of LCO|LLZO-based ASSLBs is their fast capacity fading during cycling. For instance, Tsai et al.

reported a loss of storage capacity from 1.8 mA h cm⁻² to 0.4 mA h cm⁻² (i.e. a 4.5-fold loss) within 100 cycles at 50 μ A cm⁻². Ohta et al only reported one example of LLZO-based ASSLBs that did not exhibit any significant capacity drop within 100 cycles. However, the applied current density (10 μ A cm⁻²) was too small for practical application. ²⁸

Several phenomena have been discussed as a reason for capacity fading (Figure 1). The volume variation of LCO is often considered as a reason for the LCO/LLZO interface failure and low cycling stability (Figure 1b).^{1, 3, 22} The volume change of LCO during lithiation/delithiation is around 2 vol.%. Large volumetric variation can lead to the formation of microcracks in the vicinity of the LCO/LLZO interface.²⁹ In addition, the crystal structures of LCO and LLZO are different. LCO typically has a rhombohedral structure with lattice parameters of a = 2.87 Å and c= 14.05 Å,³⁰ while the crystal structure of LLZO is cubic with a = 12.95 Å–12.97 Å.⁷ This difference might be another reason for the failure of the LCO/LLZO interface.³¹⁻³²

Another possible explanation for the low cycling stability of ASSLBs might be the electrochemical degradation of cathode/electrolyte/anode interfaces during lithiation/delithiation (Figures 1c-e). Although LLZO is believed to be stable up to 6 V vs. Li/Li⁺, recent theoretical calculations suggest that LLZO oxidation occurs already at 2.9 V vs Li/Li⁺ with the formation of poorly conductive secondary phases such as La₂Zr₂O₇ and La₂O₃.^{28, 33} At the same time, the onset of LLZO oxidation is not experimentally observed up until 5.0 V vs. Li/Li⁺, which is higher than the theoretically predicted value. This discrepancy was attributed to the high oxidation overpotential of LLZO due to kinetic limitations.³⁴ The kinetic limitations can be lower if LLZO is in contact with certainother materials. For example, Jalem et al. reported the acceleration of LLZO decomposition by carbon starting at 3.6 V vs. Li/Li⁺ with the formation of low-Li and low-oxygen LLZO, CO₂, and Li₂CO₃.³⁴

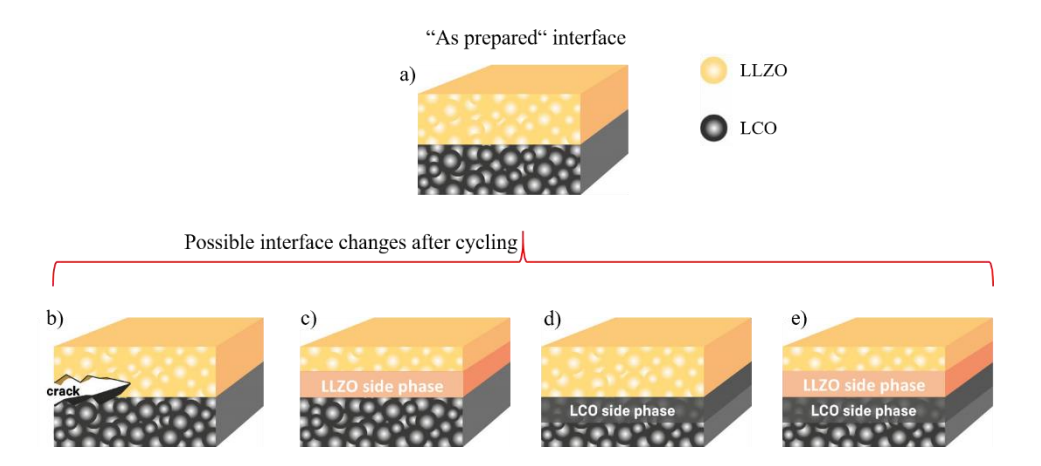


Figure 1. (a) Schematic view of the as-prepared LCO/LLZO interface. Possible reasons for the increase of LCO/LLZO interfacial impedance: (b) LCO volume change and mechanical degradation; (c) chemical or electrochemical degradation of LLZO, (d) LCO, or (e) both with the formation of secondary phases.

Besides LLZO, the electrochemical degradation of LCO can also cause capacity loss (Figure 1d). Wang et al. reported a drop in capacity caused by the disordering of the LCO/LiPON (lithium phosphorus oxynitride electrolyte) interface. ^{35–36} The disordering of LCO accompanied by a phase transformation can significantly diminish the ionic and electronic conductivity of LCO and its storage capacity. ^{30, 37} The rhombohedral crystal structure of LCO has a practical specific capacity of 140 mA h g⁻¹, ³⁰ while other LCO structures have a smaller one. The transformation of rhombohedral LCO to disordered LCO with reduced ionic and electronic conductivity leads to a significant loss in capacity. Furthermore, Otoyama et al. reported that the inhomogeneous state of charge (SoC) for LCO in a LCO-Li₂S-P₂S₅ composite cathode causes the inhomogeneous expansion/contraction of LCO, structural disordering, and interface fracturing. ³⁸

Finally, the possibility cannot be excluded that the stability of the LCO/LLZO interface depends on its lithiation state (Figure 1e).³⁹ For instance, using an atypical charge cycle of LCO between 3.0 V and 3.8 V vs. Li/Li⁺, Park et al. reported the electrochemical degradation of the LCO/LLZO

interface.²² However, the following structural characterization of electrochemically cycled LCO/LLZO interfaces did not show the existence of degradation products. Thus, experimental evidence of electrochemical decomposition in the LCO/LLZO pair is not yet available. The decomposition can be difficult to validate if the processing-induced secondary phases overlap with the products of electrochemical degradation.^{28, 33, 40}

In our study, we aimed to gain an understanding of the possible degradation mechanisms of the LCO/LLZO interface during cycling. The high-pressure FAST/SPS technique enabled the fabrication of LCO/LLZO half-cells with a chemically clean interface that is not affected by the processing-induced reaction products. Besides the plain LCO/LLZO pair, the half-cells with the LCO-LLZO composite cathode (LCO-LLZO/LLZO) were investigated. The 50/50 (wt.%) proportion between LCO and LLZO ensured the phase percolation through the bulk of the LCO-LLZO composite as well as both electronic and ionic conductivity. The composite cathode with an enlarged number and total length of the LCO/LLZO interface provided a suitable model system to study microstructural integrity and phase composition during cycling. Electrochemical impedance spectroscopy (EIS) in combination with the detailed structural characterization enabled an analysis of the mechanisms causing the interface degradation. This study can be helpful in gaining a deeper understanding of processes on the cathode/electrolyte interface in ASSLBs.

2. MATERIALS AND METHODS

Materials synthesis. Details on the synthesis of the LLZO:Ta ($\text{Li}_{6.45}\text{Al}_{0.05}\text{Zr}_{1.6}\text{Ta}_{0.4}\text{O}_{12}$) solid electrolyte and preparation of the LCO-LLZO:Ta mixture can be found elsewhere. The starting powders and LCO-LLZO:Ta mixture were stored in an Ar-filled glovebox (< 0.1 ppm H₂O and O₂).

Cell fabrication. The LCO/LLZO:Ta and LCO-LLZO:Ta half-cells were fabricated by high-pressure FAST/SPS as described in our previous paper.²² The same sintering parameters (temperature, pressure, and dwell time) were used. The possible carboreduction of LCO and LLZO:Ta during FAST/SPS was eliminated through the use of a carbon-free tool made of TZM (Mo-based alloy), the application of high mechanical pressure (440 MPa), and a low sintering temperature (750 °C). The absence of carboreduction was demonstrated by the white color of the LLZO:Ta pellets after FAST/SPS sintering.²⁵ The sintered half-cells, after polishing with SiC sandpaper, were annealed in air at 1050 °C for 30 min and then polished again. The half-cells were sputter coated with Au for 150 s (Cressington 108) on the cathode side to form the current collector and for 30 s on the LLZO: Ta side to improve the adhesion with the anode. For the anode, an In-Li composite foil was mechanically attached on the LLZO:Ta side. An In-Li anode exhibits a more stable cycling behavior and lower dendrite formation compared to the Li anodes and is stable for the electrochemical characterization parameters used.⁴² To improve the contact between the halfcell and the In-Li anode, the cells were heated to 200 °C, i.e. above the melting point of the In-Li anode, and then cooled down. The assembled full cells were placed into spring-compressed (10 N) Swagelok cells and sealed. The architecture of the full cells with the plain and composite cathode is schematically shown in Figure 2. All cells had a diameter of 12 mm and a thickness of around 0.5 mm.

Three types of cell were manufactured. The cells of the first type consisted of a plain LCO/LLZO:Ta half-cell and an In-Li anode. The second type of cell included a 35-µm-thick composite LCO-LLZO:Ta cathode, an LLZO:Ta separator, and an In-Li anode. The third type included a 170-µm-thick composite cathode. The cells with different thicknesses for the composite

cathode enabled a comparative study of the samples with different amounts and different total lengths of the LCO/LLZO:Ta interface.

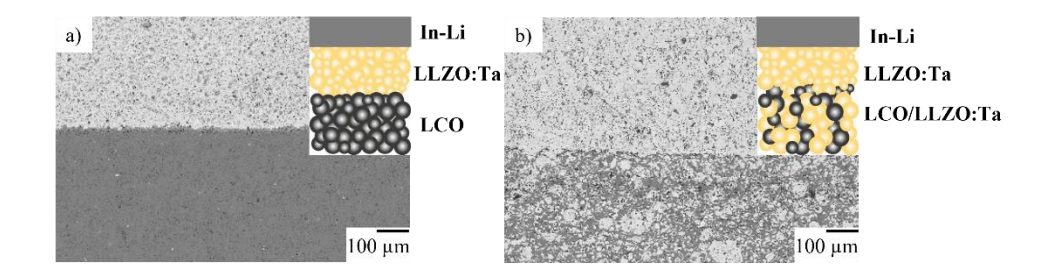


Figure 2. Cross-section and schematic overview of full cells used in this work: (a) with plain LCO cathode, and (b) with LCO-LLZO:Ta composite cathode. The dark areas are LCO and the light areas are LLZO:Ta.

Electrochemical characterization. Full cells were placed in a VT 4002EMC climate chamber (Vötsch Industrietechnik) and heated up to 80 °C. The electrochemical measurements were conducted using a BioLogic VMP-300 Potentiostat. EIS was performed in an AC field with an amplitude of 10 mV and frequencies ranging from 3 MHz to 0.1 Hz. The impedance spectra were fitted using the ZView software (Scribner). Long-term cycling was conducted using constant current/constant voltage (CC-CV) mode. The cells were charged to 3.6 V vs. In-Li (i.e., 4.2 V vs. Li/Li⁺) with a constant current density of 50 μA cm⁻² and maintained at a voltage of 3.6 V vs. In-Li until the current dropped to 10 μA cm⁻². The discharge of cells was performed with a constant current density of 50 μA cm⁻² until 2.8 V vs. In-Li.

Microstructural characterization. The microstructure was studied by means of scanning electron microscopy (SEM, Zeiss Ultra55). The SEM/EDX (energy dispersive X-ray spectroscopy) analysis was performed with an X-Max detector (80 mm², Oxford Instruments). The data were analyzed using the Inca software. The samples for transmission electron microscopy (TEM) were cut off in an FEI Helios NanoLab G3 CX instrument and transferred to a carbon lacey

TEM grid by a micromanipulator. The TEM images were recorded with a JEM-2100F (JEOL) electron microscope at 200 kV. The selected area electron diffraction (SAED) patterns were obtained using a parallel incident electron beam with a diameter of several microns. A diffracted area of the specimen was chosen with a selected-area aperture located in the image plane of the objective lens. Thus, the SAED patterns were collected from the LCO and LLZO:Ta side and their interface. TEM/EDX analysis was performed with a field emission gun equipped with a 1.2 nm electron probe. The results were analyzed with the Inca software. Phase analysis was performed by X-ray diffraction (XRD) using a D4 ENDEAVOR (Bruker) device equipped with a 1D detector (LYNXEYE). The 2θ angle varied from 10° to 80° with a step size of 0.02°. The Bragg–Brentano configuration and Cu Kα radiation were used.

Interface modeling. Thermodynamic modeling was performed to estimate the possibility of secondary phase formation between LCO and LLZO in charged states. To this end, the Al-doped cubic LLZO (Al-LLZO, only Al substitution was used to simplify the calculation) and all possible competing compounds in the Li-La-Zr-O-Co-Al-Ta set were calculated by means of the density functional theory (DFT) using the Vienna Ab initio Simulation Package (VASP).⁴³ The electronion interactions were evaluated by the projector augmented wave (PAW) method,⁴⁴ with the diffusion-correlation functional within the generalized gradient approximation of Perdew–Burke–Ernzerhof.⁴⁵ We employed Hubbard U values of 3.32 eV for Co and -1.843 eV for its corresponding formation energy correction, which were obtained by fitting the formation enthalpies to experimental results as described in the work by Jain et al.⁴⁶ All atomic coordinates were relaxed until the Hellmann–Feynman force on each atom was less than 0.01 eV/Å and the total energy difference was smaller than 10⁻⁵ eV. The wave functions were built from plane waves

with a maximum energy cutoff of 520 eV, which was tested for accuracy. The k-point mesh was set up at 2x2x2 for the Al-LLZO supercell in the Monkhorst–Pack scheme.

3. RESULTS

Cycling. Figure 3a shows the first 60 cycles of an ASSLB with a 35-μm-thick LCO-LLZO:Ta composite cathode. The first charge reveals an area-specific capacity of 1.15 mA h cm⁻² (Figure 3b). After the first discharge, the residual capacity was 0.9 mA h cm⁻². A difference in capacity of 10–20 % is typical for the first cycle of garnet-based ASSLBs.³ The first coulombic efficiency was only 78 % but increased rapidly to around 97 % within 15 cycles. The areal capacity of the cell in question stabilized after around 45 cycles at 0.3 mA h cm⁻². In comparison, the plain LCO-cathode configuration has a much lower areal capacity of 0.03 mA h cm⁻² (Figure S1). This value is in line with the data reported by other authors.^{48, 50}

As expected, the increase in thickness of the LCO-LLZO:Ta composite cathode results in a higher areal capacity. Figure 3c shows the cycling results for a cell with a thick LCO-LLZO:Ta composite cathode (170 μm). The first charge was 6 mA h cm⁻² (Figure 3d). After the first discharge, the cell revealed a significant capacity loss of nearly 2 mA h cm⁻². The related discharge capacity was 4 mA h cm⁻² and the initial coulombic efficiency was 66 %, which is much lower than for the cell with the thin LCO-LLZO:Ta composite cathode (78 %). Within the first four cycles, the coulombic efficiency increased to 85 % in the thick LCO-LLZO:Ta composite cathode. However, in the fifth cycle, a coulombic efficiency of just 75 % was achieved.

In summary, the cell with a thick LCO-LLZO:Ta composite cathode showed much larger degradation than the cell with a thin composite cathode. This can be attributed to the larger amount and total length of the LCO/LLZO:Ta interfaces in the thick composite cathode. This observation

is an important indicator of the crucial influence of interface degradation on the performance of ASSLBs.

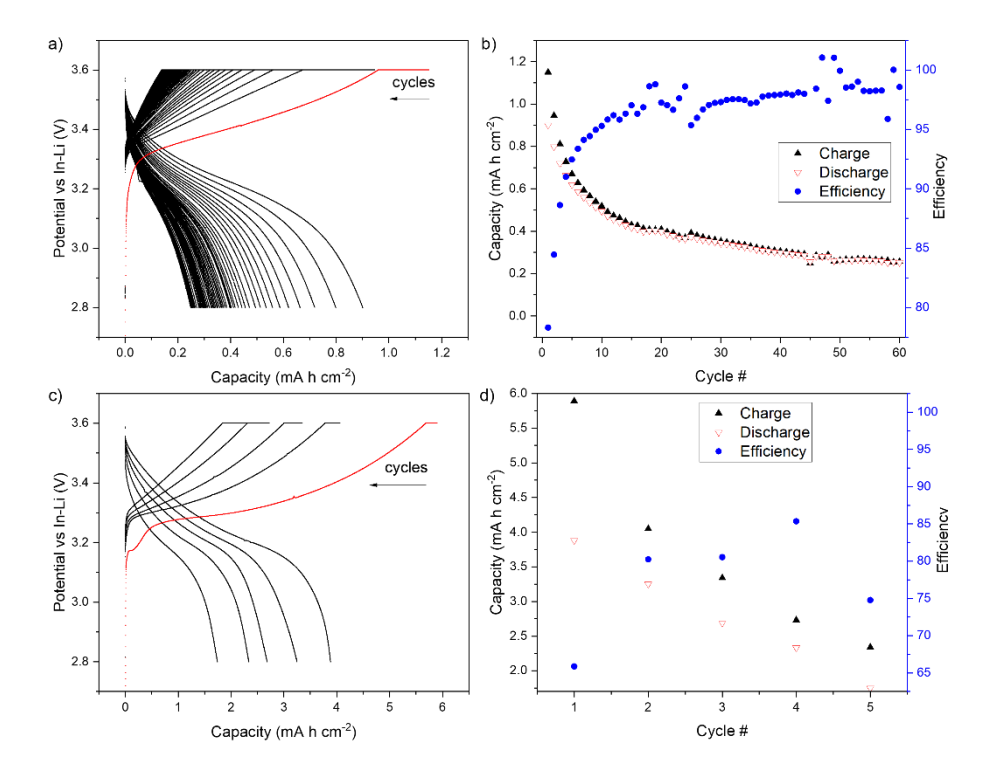


Figure 3. (a, c) Charge/discharge curves; (b, d) capacity and coulombic efficiency for (a, b) cells with a thin LCO-LLZO:Ta cathode and (c, d) a thick LCO-LLZ:Ta cathode. The first charge is shown in red.

Impedance. Figures 4a and b show the Nyquist plot for electrochemical impedance measured at 80°C for cells with a plain and a thick LCO-LLZO:Ta composite cathode. Both Nyquist plots show the semicircle at high frequencies attributed to the total (bulk, and grain boundary) resistance of the electrolyte, and the stretched semicircle in the mid- to low-frequency range. The latter semicircle in ASSLBs is typically interpreted as a superposition of individual impedances of the anode and cathode. Figure 4c shows the equivalent circuit used for fitting of impedance spectra.

For the LCO|LLZO:Ta|In-Li cell with a plain LCO cathode (Figure 4a), a bulk resistance of $33 \Omega \text{ cm}^2$ and a grain boundary resistance of $44 \Omega \text{ cm}^2$ were found after the first charge (Table 1).

These values are similar to the impedance of an individual LLZO: Ta layer, which revealed a bulk resistance of 22 Ω cm² and a grain boundary resistance of 51 Ω cm² (Figure S2). The LLZO:Ta impedance in the LCO|LLZO:Ta|In-Li cell increased slightly after the fifth charge. While the bulk impedance of LLZO:Ta remained the same, indicating the stability of the LLZO:Ta grains, the grain boundary contribution increased slightly to $47 \Omega \text{ cm}^2$ after five charges. Since the LCO|LLZO:Ta|In-Li cell has geometrically well-defined interfaces, the impedance of the negative and positive electrode can be considered to be the interfacial impedance of the respective electrode. The fitting of the associated semicircle in the frequency range from 5 kHz to 100 mHz resulted in an impedance of 195 Ω cm² for the LCO/LLZO: Ta interface after the first charge, which increased to $260 \Omega \text{ cm}^2$ after the fifth charge. Compared to the LCO/LLZO: Ta interface, the impedance of the LLZO:Ta/In-Li interface is much lower at just 25 Ω cm² after the first charge. The anode impedance even decreased after cycling, reaching 15 Ω cm² after the fifth charge. The obtained initial values are in good agreement with the reported interfacial impedance for LCO/LLZO:Ta (around 170 Ω cm² at RT) and for the LLZO:Ta/In-Li interface (25–28 Ω cm² at RT).⁷ Thus, the observed increase of impedance in the LCO|LLZO:Ta|In-Li cell can be attributed to the degradation of the LCO/LLZO:Ta interface.

The Nyquist plot for the LCO-LLZO:Ta|LLZO:Ta|In-Li cell with a composite cathode appears qualitatively similar. However, its total impedance was significantly higher (Figure 4b). The values of bulk and grain boundary resistance (35 Ω cm² and 79 Ω cm², respectively) are only slightly higher than those for the LCO|LLZO:Ta|In-Li cell (Table 1). It is worth noting that the bulk LLZO:Ta resistance remained constant during cycling, while the grain boundary resistance increased after five charges from 79 Ω cm² to 112 Ω cm². The major increase in total impedance results from the impedance of the cathode/separator interface, which increased by over 70 % from

an initial $1081 \,\Omega\,\text{cm}^2$ to $1854 \,\Omega\,\text{cm}^2$ after five charges. We can assume that the larger LCO/LLZO:Ta interface area (normalized on the geometric area) in the composite cathode leads to increased interfacial impedances. This statement is supported by Song et al., who reported an increase in total interfacial impedance for cathodes with an enhanced thickness.⁵¹ In addition, the larger amount of interface in the LCO-LLZO:Ta cathode resulted in a significantly higher increase in impedance after cycling compared to the plain LCO cathode. The increase in impedance might be a result of the mechanical or electrochemical degradation of the LCO/LLZO:Ta interface.

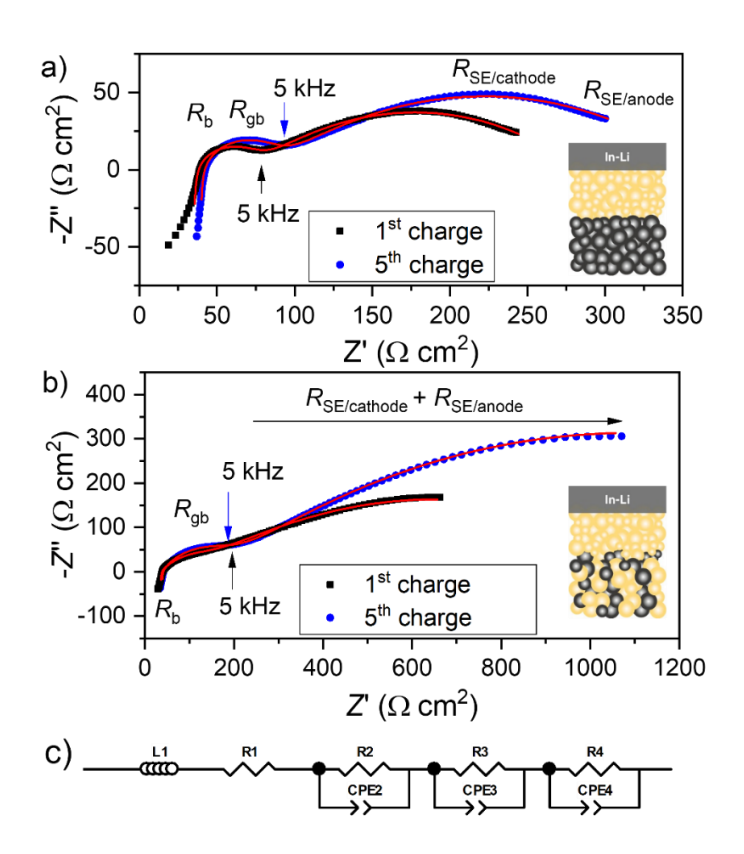


Figure 4. Nyquist plot after first and fifth charge for cells with (a) a plain LCO cathode and with (b) a LCO-LLZO: Ta composite cathode. In the equivalent circuit (c): L is the inductance, R is the ohmic resistance, and CPE is the constant phase element.

Table 1. Fitted areal resistivity (Ω cm²) for cells with a plain LCO and a thick LCO-LLZO:Ta composite cathode after first and fifth charge.

Place	LCO		LCO-LLZO:Ta	
	1 st charge	5 th charge	1 st charge	5 th charge
Bulk	33	33	35	35
Grain boundary	44	47	79	112
LCO/LLZO:Ta	195	260	1081	1854
LLZO:Ta/In-Li	25	15	25	15

4. DISCUSSION

Mechanical degradation. Mechanical degradation due to volume variation during lithiation/delithiation is the most common explanation for capacity fading in LCO-based cathodes (Figure 1b).^{3, 54-55} In our previous paper, we observed the formation of cracks in porous LCO-LLZO:Ta cathodes with a porosity of about 20 %. 26 We observed several micrometer-sized cracks between the LCO and LLZO grains as well as the intragranular fracturing of LCO after cycling. However, in this work we did not find any traces of mechanical degradation either before or after cycling in dense LCO-LLZO: Ta cathodes fabricated by FAST/SPS. The SEM images in Figures 5a and b show that the LCO-LLZO: Ta composite cathode was dense and did not have any mechanical defects either before or after cycling. The images with lower magnification demonstrate the homogeneous microstructure of LCO-LLZO:Ta composite cathodes with a density of around 95 % (Figure S3). In general, the SEM images confirm the homogeneous distribution of LCO and LLLZO:Ta grains throughout the cathode. The interface between grains appears sharp and well sintered, without visible reaction zones or microcracks (Figure 5a and Figure S3a). The cycled LCO-LLZO: Ta composite cathodes showed the same morphology and mechanical stability throughout the whole thickness (Figure 5b and Figure S3b). In contrast to porous LCO-LLZO:Ta cathodes,²⁶ no macro- or microcracks were observed for cycled dense

composite cathodes. We believe that a high density achieved via FAST/SPS is beneficial for the mechanical stability of LCO-LLZO:Ta cathodes during cycling.

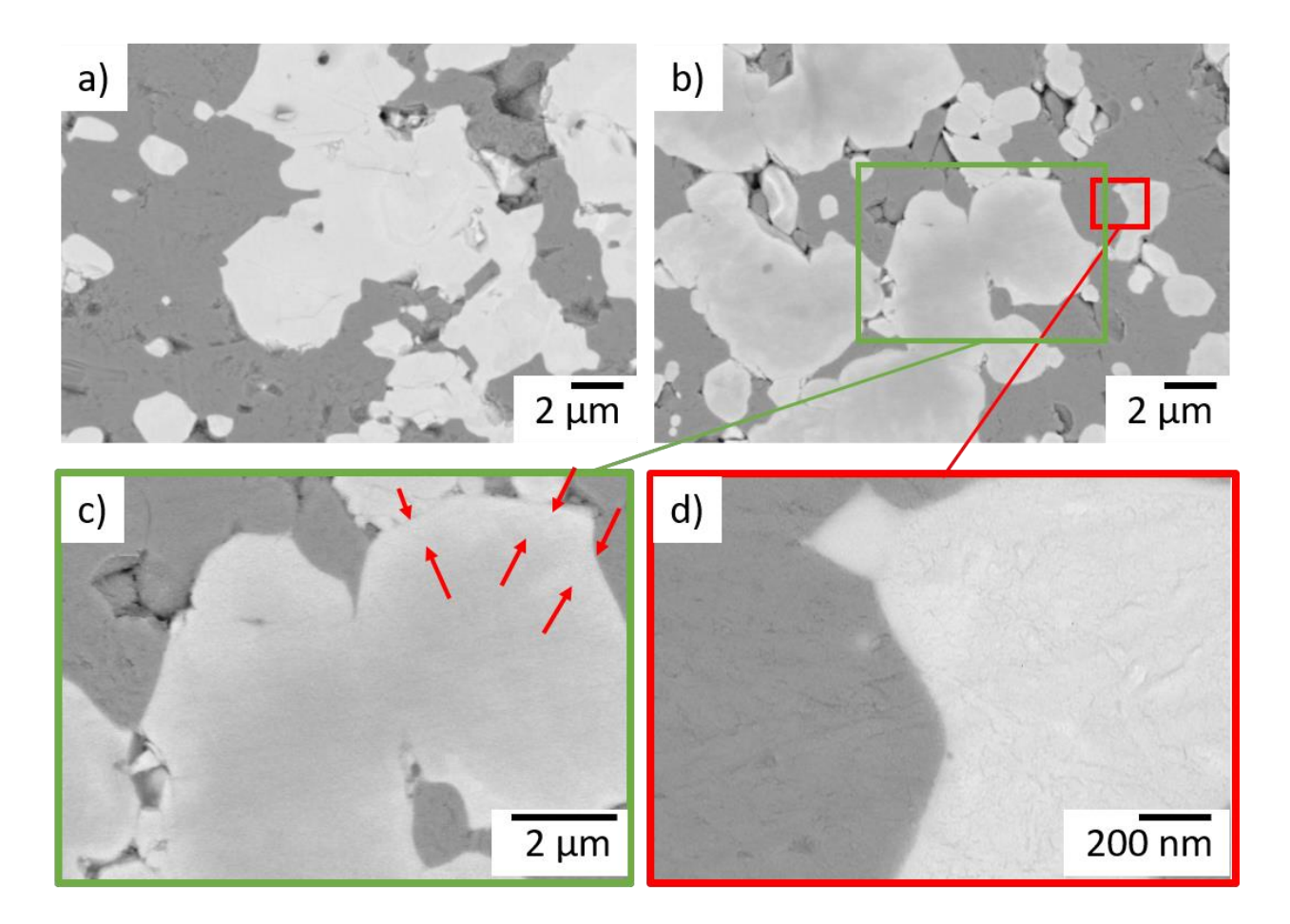


Figure 5. Cross-section of LCO-LLZO:Ta composite cathode (a) before and (b) after cycling. The bright areas represent LLZO:Ta, the dark areas LCO; the pores are black. (c) The higher resolution reveals the formation of bright rims in LLZO:Ta grains in contact with LCO after cycling (red arrows). (d) High-resolution image of the same composite cathode shows the mechanical stability of the LCO/LLZO:Ta interface after cycling.

The formation of nano-sized cracks can also be ruled out for the discussed LCO/LLZO:Ta interface, as the TEM results (Figures 6a and d) do not show any cracks or other signs of mechanical degradation. In conclusion, it is very unlikely that mechanical failure (if any) of the

LCO/LLZO:Ta interface is responsible for a 60 % loss of capacity in the LCO-LLZO:Ta|LLZO:Ta|In-Li cell (Figure 3d), as this would mean the cracking of a similar amount of interface, which was not observed either by SEM or by TEM (Figures 5 and 6).

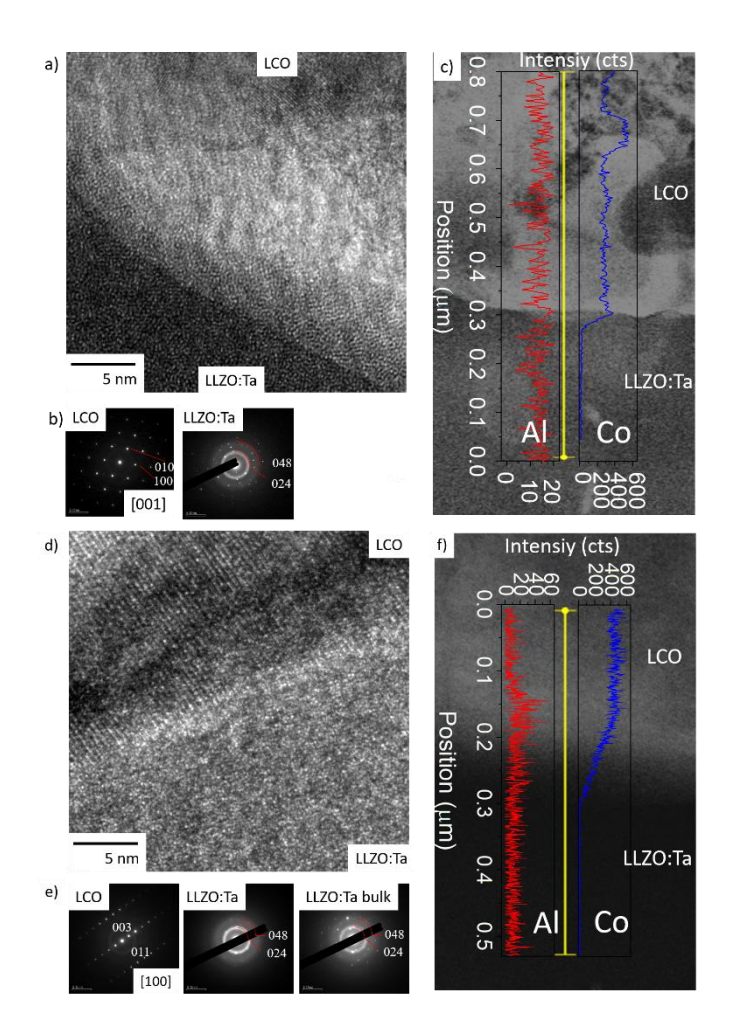


Figure 6. TEM images of (a) as-prepared and (d) cycled LCO/LLZO:Ta interface. (b) SAED patterns of the LCO and LLZO:Ta phases for the as-prepared composite cathode and (e) after cycling. Figure S4 shows the location of the investigated area. Figures 6c and f show the TEM/EDX lines for the distribution of Al and Co across the interface.

To the best of our knowledge, this is the first time that the LCO/LLZO:Ta interface has been proven to be mechanically stable during cycling. Understanding this phenomenon requires special

chemo-electric-mechanical analysis considering all associated properties of LCO and LLZO:Ta, properties of the LCO/LLZO:Ta interface, the charging and discharging cycles, and probably the thermal history of the interface. The obvious advantage of a FAST/SPS-sintered dense cathode and interface over a free-sintered porous one is the absence of pores or the reduction in porosity. Pores induce stress localization and promote the LCO/LLZO:Ta interface fracturing.^{49, 56}

Processing-induced degradation. Processing-induced degradation with the formation of a secondary phase at elevated temperatures is another common explanation for storage capacity fading. ^{39, 52–53} However, SEM and TEM analysis of the sintered samples (Figures 5 and 6) show that a major part of the LCO/LLZO:Ta interfaces after FAST/SPS processing is chemically clean and does not feature any reaction zones. It can therefore be concluded that the reaction products might only form a few separated domains and not continuous interfacial layers (Figure 5a). Even if the LCO/LLZO:Ta interface has a certain amount of the processing-induced secondary phase, this phase cannot significantly affect the electrochemical performance of the investigated cells or be responsible for a continuous loss of capacity and increase in impedance while cycling (Figures 3 and 4).

Electrochemical degradation. Although we did not see mechanical degradation of the LCO-LLZO:Ta composite cathode and LCO/LLZO:Ta interface, the results of SEM and TEM investigations (Figures 5 and 6) demonstrate the influence of cycling on the microstructure of LCO, LLZO:Ta, and the LCO/LLZO:Ta interface. The changes are especially noticeable around the LCO/LLZO:Ta interface. The SEM images reveal a contrast gradient in LLZO:Ta grains after cycling. The LLZO:Ta grains, which initially have a uniform bright contrast (Figure 5b), exhibit a bright rim of around 0.3 μm at the interface with LCO after cycling (Figure 5c). The high-resolution TEM observation prior to cycling reveals an ordered crystal structure of LCO and

LLZO:Ta grains with a sharp interface (Figure 6a). The selected area electron diffraction (SAED) pattern for LLZO:Ta (Figure 6b) only shows the reflections corresponding to the polycrystalline cubic LLZO:Ta with a lattice parameter of around 12.9 Å. This value is in the range reported for cubic LLZO (12.95 Å–12.97 Å)⁷. The ordered crystal structure was also found for LCO. The SAED pattern in Figure 6b reveals the rhombohedral crystal structure ($R\overline{s}m$) with lattice parameters of a=2.80 Å and c=13.99 Å. These values are in good agreement with the data for LCO in the literature (a=2.81 Å and c=14.05 Å)³⁰. TEM/EDX analysis shows the clear edge for the distribution of Co and La on the LCO/LLZO:Ta interface (Figure 6c and Figure S5). The signal for Al is hidden in the background (Figure 6c).

While LCO and LLZO:Ta grains have a crystal structure and a well-defined interface before cycling, the cycled LCO/LLZO:Ta interface appears different (Figure 6d). The SAED patterns exhibit an amorphous (disordered) LLZO:Ta microstructure in the vicinity of the cycled LCO/LLZO:Ta interface, while the bulk retains the crystalline microstructure (Figure 6e). The thickness of the disordered LLZO:Ta layer is around 0.1 µm. This observation is in agreement with the SEM images in Figures 5b and c. Disordered LLZO exhibits low ionic conductivity and might form a Li-ion blocking layer covering the majority of the LCO/LLZO:Ta interface. ^{3,7} Disordering of the LLZO:Ta layer is one possible explanation for the high interfacial impedance and fading capacity, especially as the SAED cannot exclude the formation of a secondary phase within disordered LLZO:Ta and a reduction of the Al molar amount within LLZO:Ta.

The LCO grains also exhibit a certain change after cycling. Although LCO retains the crystal structure, two phases were detected by SAED after cycling. In addition to the parent rhombohedral LCO, the SAED pattern shows some satellite peaks (Figure 6e). The lattice parameters of the secondary phase are in good agreement with LCO substituted by Al (LCO: a=2.814 Å, c=1.00 km secondary phase are in good agreement with LCO substituted by Al (LCO: a=1.00 km secondary phase are in good agreement with LCO substituted by Al (LCO: a=1.00 km secondary phase are in good agreement with LCO substituted by Al (LCO: a=1.00 km secondary phase are in good agreement with LCO substituted by Al (LCO: a=1.00 km secondary phase are in good agreement with LCO substituted by Al (LCO: a=1.00 km secondary phase are in good agreement with LCO substituted by Al (LCO: a=1.00 km secondary phase are in good agreement with LCO substituted by Al (LCO: a=1.00 km secondary phase are in good agreement with LCO substituted by Al (LCO: a=1.00 km secondary phase are in good agreement with LCO substituted by Al (LCO: a=1.00 km secondary phase are in good agreement with LCO substituted by Al (LCO: a=1.00 km secondary phase are in good agreement with LCO substituted by Al (LCO: a=1.00 km secondary phase are in good agreement with LCO: a=1.00 km secondary phase are in good agreement with LCO: a=1.00 km secondary phase are in good agreement with LCO: a=1.00 km secondary phase are in good agreement with LCO: a=1.00 km secondary phase are in good agreement with LCO: a=1.00 km secondary phase are in good agreement with LCO: a=1.00 km secondary phase are in good agreement with LCO: a=1.00 km secondary phase are in good agreement with LCO: a=1.00 km secondary phase are in good agreement with LCO: a=1.00 km secondary phase are in good agreement with LCO: a=1.00 km secondary phase are in good agreement with LCO: a=1.00 km secondary phase are in good agreement with LCO: a=1.00 km secondary phase are in good agree

14.048 Å vs. LiCo_{1-x}Al_xO₂: a = 2.81 Å, c = 14.08 -14.10 Å (x \leq 0.2))⁵⁷. The presence of Al in LCO after cycling was also detected via TEM/EDX (Figure 6f and Figure S6).

The TEM/EDX and – to a certain extent – SEM/EDX of the LCO/LLZO: Ta interface reveal the presence of Co within LLZO: Ta after cycling (Figure 6f, and Figures S6 and S7). A certain amount of Al is also detected within LCO after cycling (Figure 6c and Figure S8). An interchange between Al and Co atoms during cycling can be expected due to the same oxidation state (+3) and comparable ionic radii (A13+: 67.5 pm, Co3+: 68.5 pm). The increased average atomic mass of Cosubstituted LLZO:Ta in the vicinity of the LCO/LLZO:Ta interface explains the brighter contrast in SEM and supports the TEM/EDX data. However, a certain amount of Co diffuses into the bulk of LLZO:Ta (Figures 5b and c, and Figure S7). As the LiAlO₂ coating improves the cycling stability of the cathode active materials, ^{58–59} we can assume that the formation of the LiCo_{1-x}Al_xO₂ $(x \le 1)$ phase might be beneficial for LCO electrochemical properties. However, in garnet-based ASSLBs, the electrochemical performance limitations result from LLZO and thus diminish a possible improvement of LCO performance.⁴⁹ The diffusion of cobalt into LLZO is commonly considered to be a negative side effect during the high-temperature processing of the LCO-LLZO couple.^{3, 7, 60} However, in FAST/SPS sintered samples, we did not observe the brighter spots in the LLZO:Ta area before cycling (Figure 5a). The low-temperature FAST/SPS clearly prevents elemental diffusion during sintering.²⁵ However, Al and Co diffuse during cycling and lead to an increase in interfacial impedance. This may be related (at least partly) to the stresses appearing around the LCO/LLZO: Ta interface during cycling. As the stresses are not released by fracturing of the LCO/LLZO: Ta interface, the secondary phase formation can occur with Co diffusion into the LLZO:Ta lattice. 61-62 The Co ions within the LLZO:Ta can be considered to be electrochemically active with the change of its oxidation state (+3 and +4) while cycling. The

oxidation state changes cause the change of Co ionic radii and disordering within LLZO:Ta. As disordered LLZO has low Li-ion conductivity, a Li-ion blocking layer forms at the LCO/LLZO:Ta interface during cycling. In addition, the loss of Al substitution in LLZO:Ta can lead to the formation of the tetragonal LLZO:Ta with low ionic conductivity or other even non-Li-ion conductive secondary phases.^{22, 63}

To gain further insight into the phase composition, XRD patterns at various locations of the LCO-LLZO:Ta composite cathodes were recorded before and after 5 cycles in the discharged state (Figures S9 and S10). The as-prepared LCO-LLZO:Ta composite cathode shows sharp reflections corresponding to a mixture of crystalline LCO and LLZO:Ta phases. A similar XRD pattern revealed the back side of the cycled composite cathode. To access the area closer to the separator, a layer of composite cathode was removed by polishing (Figure S10). However, we did not find new reflections related to decomposition products in this part of the LCO-LLZO:Ta cathode. Thus, if any decomposition of LCO or LLZO:Ta occurs, it is in a thin layer at the LCO/LLZO:Ta interface, as indicated by TEM analysis (Figure 6). For LCO, Rietveld analysis revealed an unchanged crystal structure throughout the LCO-LLZO:Ta composite cathode (back: a=2.815 Å, c=14.06 Å and interface: a=2.817 Å, c=14.06 Å). These values are in good agreement with the data reported for LCO (a=2.81 Å, c=14.05 Å) a=14.06 Å0. However, the Al substitution seen in TEM/EDX (Figures 6c to f) is hardly detectable by XRD due to similar lattice parameters of LCO and LiCo_{1-x}Al_xO₂ (LiCo_{1-x}Al_xO₂: a=2.81 Å, c=14.08 -14.10 Å, and $x \le 0.2$) a=1.00 Å5.

In LLZO:Ta, a significant decrease in crystalline domain size from 90 nm to 20 nm was found via Rietveld analysis for the interface region. This supports the SAED-observed disordering of LLZO:Ta after cycling (Figure 6d). The smaller crystalline domain size and the structural changes result in the enhanced total length of the LLZO:Ta grain boundaries and in the disordering of the

microstructure. Both these factors contribute to a decline in ionic conductivity in LLZO:Ta.⁶⁴ The XRD patterns of the non-cycled LCO-LLZO:Ta composite cathodes are consistent throughout the entire thickness range (Figure S9). This excludes the preparation procedure as a source of structural disordering. Hence, the decrease in crystalline domain size observed by XRD in cycled LLZO:Ta can be attributed – as an exception – to an electrochemically induced phenomenon.

One of the reasons for the LCO/LLZO:Ta interface change could be the electrochemical decomposition of LLZO:Ta at potentials of above 2.9 V (vs Li/Li⁺) as calculated by Han et al.²⁸ This scenario is unlikely as the suggested degradation products were not found, which is likely due to the high oxidation overpotential of LLZO (above 5.0 V vs Li/Li⁺) or due to kinetic limitations.³⁴ In addition, the bulk impedance of LLZO:Ta remains constant during cycling and only the grain boundary impedance increases. This observation suggests an alteration of only the grain boundaries (Figure 4 and Table 1).

Thermodynamics of interfaces. Since the interdiffusion of Al and Co ions after cycling appeared over the LCO/LLZO:Ta interface, we can state that both LCO and LLZO:Ta change the chemical composition in the vicinity of the LCO/LLZO:Ta interface. To analyze possible reasons for the interface change, we calculated the reaction energy for the possible formation of secondary phases, assuming the mobility of the Al and Co ions. Since no decomposition products of LLZO:Ta were detected at the LCO/LLZO:Ta interface, the simulation was used to support the assumption of Al and Co diffusion. The Al and Co diffusion between LCO and LLZO:Ta during thermal processing has been reported previously and was regarded as a reason for high interfacial impedance.²² However, in this work, the Al and Co diffusion was more a result of electrochemical cycling.

Using the DFT calculation, the reaction energies of LCO and Al-LLZO (Li_{6.625}Al_{0.125}La₃Zr₂O₁₂) against their competing phases were calculated to evaluate the LCO/Al-LLZO interfacial stability in relation to the LCO lithiation state. Applying the condition of thermodynamic stability (lowest formation energy of a constituent), and the self-developed MATLAB code to competing compounds of the Li-La-Zr-O-Co-Al-Ta system (Table S1), the interfacial reaction energy was calculated at different states of charge (SoC) (Figures 7 and S11).

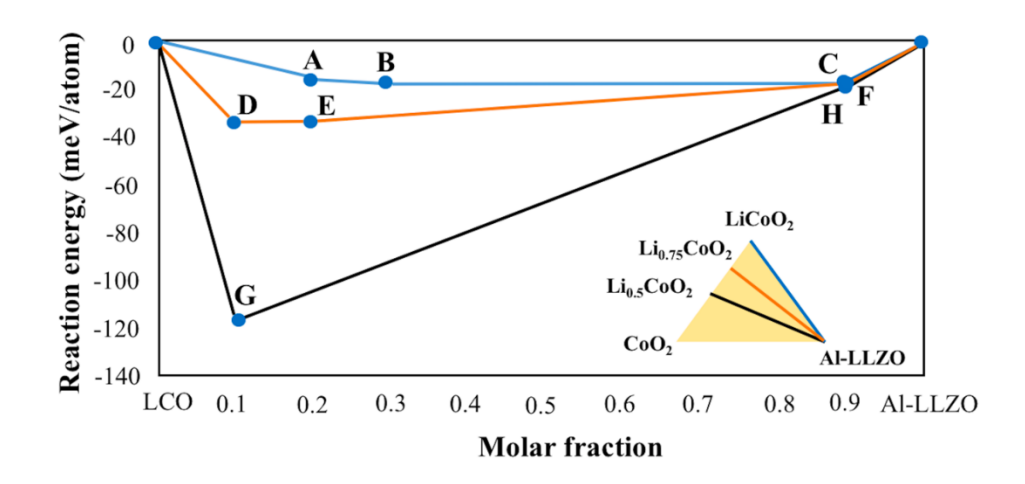


Figure 7. LCO vs. Al-LLZO pseudo-binary phase diagram at different states of charge. Blue circles indicate the possible decomposition products.

The reaction energy is strongly dependent on the SoC. The energy becomes much lower in the half-charged state compared to the discharged state. This shows that low conductive interphases formed more easily in the charged state. The corresponding competing phases for various SoCs are listed in Table 2 (with more details in Table S2). In particular, the diffusion of Al from Al-LLZO into LCO takes place with reaction G stabilizing LLZO and Al-LCO at the interface. Based on the results in Table 1 and Table S3, Al substitution can be predicted in LCO at every SoC. This is in good agreement with our experimental observation (Figures 6c, S6, S7).

As secondary phases were not experimentally seen between Al-LLZO and LCO after processing (i.e. in the fully discharged state), we can assume that the formation of secondary phases is kinetically hindered. This can also be justified by the fact that the calculated total energies of products A, B, and C are only slightly lower than those of reactants in the fully discharged state, namely Al-LLZO and LiCoO₂. However, our DFT calculation shows that the products of reaction G are significantly more favorable than their corresponding reactants, namely Al-LLZO and the half-charged LCO, demonstrating that the formation of low- or non-Li-conductive secondary phases becomes more possible with cycling. For Ta and Al co-substituted LLZO (Li_{6.25}Al_{0.125}La₃Ta_{0.375}Zr_{1.625}O₁₂), a similar result is expected with the appearance of new competing phases such as La₃TaO₇ and Li₅TaO₅. It is worth mentioning that La and Ta are heavy elements that are presumed to be immobile in the system. Thus, their related compounds are unlikely to form at the interface.

Table 2. Thermodynamically possible phases at the LCO/Al-LLZO interface for different states of charge from fully discharged (LiCoO₂) to half-charged (Li_{0.5}CoO₂), as shown in Figure 7.

Interface	ID	Competing phases
LiCoO ₂ Al-LLZO	A	Al-LCO, LLZO, La ₂ Zr ₂ O ₇ , Li ₅ CoO ₄ , LaCoO ₃
	В	Al-LCO, LLZO, La ₂ Zr ₂ O ₇ , Li ₅ CoO ₄ , La ₄ Al ₂ O ₉
Li _{0.75} CoO ₂ Al-LLZO	C	LLZO, LiAlO ₂ , La ₄ Al ₂ O ₉ , La ₂ Zr ₂ O ₇ , Li ₅ CoO ₄
	D	$\textbf{Al-LCO},La_2Zr_2O_7,Li_5CoO_4,LaCoO_3,Li_6CoO_4,Li_7Co_5O_{12}$
	E	Al-LCO, LLZO, La ₄ Al ₂ O ₉ , La ₂ Zr ₂ O ₇ , Li ₂ CoO ₃ , LaCoO ₃
	F	LLZO, LiAlO ₂ , La ₄ Al ₂ O ₉ , La ₂ Zr ₂ O ₇ , Li ₅ CoO ₄ , Li ₂ CoO ₃
Li0.5CoO ₂ Al-LLZO	G	Al-LCO, La ₂ Zr ₂ O ₇ , Li ₂ CoO ₃ , LaCoO ₃ , Li ₇ Co ₅ O ₁₂ , CoO ₂
	Н	LLZO, LiAlO ₂ , La ₄ Al ₂ O ₉ , La ₂ Zr ₂ O ₇ , Li ₅ CoO ₄ , Li ₂ CoO ₃

Summary and Outlook. As we did not observe mechanical degradation, the reversible cycling of LCO/LLZO:Ta can be assumed. However, the results of electrochemical characterization, material characterization of the interface, and the modeling results clearly demonstrate the electrochemically driven degradation of the LCO/LLZO:Ta interface. The interface degradation is caused by phase composition modification on both LLZO:Ta and LCO sides due to Co and Al substitution and amorphization. The observed participation of Al-substitute ions from LLZO:Ta in the electrochemically driven phase transformation processes is surprising. This occurrence has not been considered before. Our calculations and experimental observations suggest that aluminum – although not redox-active – plays a significant role in observed phase transformations, enabling the migration of Co ions in the LLZO:Ta phase. However, it is also possible that Co migrates into LLZO:Ta and replaces three Li ions. This would allow more Co diffusion into LLZO:Ta than if only by the replacement of Al ions. The enhanced diffusion of Co can significantly accelerate the degradation of the LCO/LLZO:Ta interface.

Applying an interfacial layer could mitigate the observed degradation. However, the interlayers, such as LiBO₃ or LiNbO₃, could cause high impedance and limit electrochemical performance due to relatively low Li-ion conductivity. ^{66–67} A thorough interface layer design is needed to prevent the degradation of the LCO/LLZO:Ta interface, while retaining good Li-ion conductivity. Another approach would be the replacement of the cathodic material. A feasible alternative could be Li_aNi_xMn_yCo₂O₂ (NMC) with a reduced Co content or Co-free materials such as LiNi_{0.5}Mn_{1.5}O₄ (LMNO) or LiFePO₄ (LFP). However, the optional interlayers or a different CAM-LLZO:Ta pair require a detailed study before a conclusive answer can be provided on their resistivity against degradation.

5. CONCLUSIONS

In the present study, the degradation of the LCO/LLZO:Ta interface during electrochemical cycling was studied. The study was performed on the plain LCO|LLZO:Ta|In-Li cell and on the cell with a composite cathode (LCO-LLZO:Ta|LLZO:Ta|In-Li). The high-pressure FAST/SPS in a metallic mold enabled the fabrication of both half-cells without secondary phase formation and with nearly full densification of the layers. The half-cells were assembled with an In-Li anode and were electrochemically evaluated. The more rapid fading of storage capacity for the cell with an LCO-LLZO:Ta composite cathode predominantly shows degradation at the LCO/LLZO:Ta interface. This observation was confirmed by electrochemical impedance spectroscopy. SEM and TEM investigations of the LCO/LLZO:Ta interface did not reveal any traces of its mechanical degradation. At the same time, TEM and SAED analysis revealed the amorphization of the LCO/LLZO:Ta interface. Furthermore, the diffusion of Co from LCO into LLZO:Ta and Al from LLZO:Ta into LCO was detected. The intercalation of Co into the LLZO:Ta lattice might be a reason for the disordering of the LCO/LLZO:Ta interface with the degradation of Li-ion conductivity. Further, thermodynamic analysis, using the density functional theory, confirmed the possibility of Al diffusion during cycling combined with the formation of low-conducting secondary phases.

ASSOCIATED CONTENT

Supporting Information

The Supporting Information is available free of charge at the ACS Applied Materials & Interfaces website.

The Supporting Information includes: the charge/discharge curves for LCO|LLZO:Ta|In-Li cell; the Nyquist plot of LLZO:Ta separator at 80 °C; SEM and TEM images of LCO-LLZO:Ta|LLZO half-cell and LCO/LLZO:Ta inteface; TEM/EDX scans across LCO/LLZO:Ta interface;

SEM/EDX spectra on LCO and LLZO: Ta side before and after cycling; XRD patterns of uncycled and cycled composite cathode; the LCO vs. Al-LLZO pseudo-binary phase diagram at a SoC of 75% and 100%; tables with calculated formation energies of competing compounds in Li-La-Zr-O-Co-Al-Ta system, related reactions and thermodynamically possible compounds at a charge of 75% and 100%...

AUTHOR INFORMATION

Corresponding Authors

Martin Ihrig – Institute of Energy and Climate Research – Materials Synthesis and Processing, Forschungszentrum Jülich GmbH, 52425 Jülich, Germany; tel: +49-2461-6196841; email: m.ihrig@fz-juelich.de; Fax: +49-2461-619120

Martin Finsterbusch – Institute of Energy and Climate Research – Materials Synthesis and Processing, Forschungszentrum Jülich GmbH, 52425 Jülich, Germany; email: m.finsterbusch@fz-juelich.de

Dina Fattakhova-Rohlfing – Institute of Energy and Climate Research – Materials Synthesis and Processing, Forschungszentrum Jülich GmbH, 52425 Jülich, Germany; email: d.fattakhova@fz-juelich.de

Present Address

†Alexander M. Laptev is now with the Łukasiewicz Research Network – Poznań Institute of Technology, 6 Ewarysta Estkowskiego St., 61-755 Poznan, Poland

Notes

The authors declare no competing financial interest.

ACKNOWLEDGMENT

The financial support provided by the Federal Ministry of Education and Research (Bundesministerium für Bildung und Forschung), Germany, projects no 13XP0134A (EvaBatt), 13XP0305A (AdamBatt), and 13XP0223A (CatSE) and by the Ministry of Science and Technology, Taiwan, projects no. 109-2636-E-006-012, and 110-2636-E-006-016 is gratefully acknowledged.

REFERENCES

- 1) Xiao, Y.; Wang, Y.; Bo, S.-H.; Kim, J. C.; Miara, L. J.; Ceder, G. Understanding Interface Stability in Solid-State Batteries. *Nat. Rev. Mater.* **2020,** *5* (2), 105-126. DOI: 10.1038/s41578-019-0157-5.
- (2) Janek, J.; Zeier, W. G. A Solid Future for Battery Development. *Nat. Energy* **2016**, *1*, No 16141. DOI: 10.1038/Nenergy.2016.141.
- (3) Wang, C.; Fu, K.; Kammampata, S. P.; McOwen, D. W.; Samson, A. J.; Zhang, L.; Hitz, G. T.; Nolan, A. M.; Wachsman, E. D.; Mo, Y.; Thangadurai, V.; Hu, L. Garnet-Type Solid-State Electrolytes: Materials, Interfaces, and Batteries. *Chem. Rev.* **2020**, *12* (10). DOI: 10.1021/acs.chemrev.9b00427.
- (4) Zhao, N.; Khokhar, W.; Bi, Z.; Shi, C.; Guo, X.; Fan, L.-Z.; Nan, C.-W. Solid Garnet Batteries. *Joule* **2019**, *3* (5), 1190-1199. DOI: 10.1016/j.joule.2019.03.019.
- (5) Wolfenstine, J.; Allen, J. L.; Sakamoto, J.; Siegel, D. J.; Choe, H. Mechanical Behavior of Li-Ion-Conducting Crystalline Oxide-Based Solid Electrolytes: A Brief Review. *Ionics* **2018**, *24* (5), 1271-1276. DOI: 10.1007/s11581-017-2314-4.

- (6) Thangadurai, V.; Narayanan, S.; Pinzaru, D. Garnet-Type Solid-State Fast Li Ion Conductors for Li Batteries: Critical Review. *Chem. Soc. Rev.* **2014**, *43* (13), 4714-27. DOI: 10.1039/c4cs00020j.
- (7) Samson, A. J.; Hofstetter, K.; Bag, S.; Thangadurai, V. A Bird's-Eye View of Li-Stuffed Garnet-Type Li₇La₃Zr₂O₁₂ Ceramic Electrolytes for Advanced All-Solid-State Li Batteries. *Energy Environ. Sci.* **2019**, *12* (10), 2957-2975. DOI: 10.1039/C9EE01548E.
- (8) Rawlence, M.; Garbayo, I.; Buecheler, S.; Rupp, J. L. M. On the Chemical Stability of Post-lithiated Garnet Al-stabilized Li₇La₃Zr₂O₁₂ Solid State Electrolyte Thin Films. *Nanoscale* **2016**, *8* (31), 14746-14753. DOI: 10.1039/C6NR04162K.
- (9) Ihrig, M.; Mishra, T. P.; Scheld, W. S.; Häuschen, G.; Rheinheimer, W.; Bram, M.; Finsterbusch, M.; Guillon, O. Li₇La₃Zr₂O₁₂ Solid Electrolyte Sintered by the Ultrafast High-Temperature Method. *J. Eur. Ceram. Soc.* **2021**, *41* (12), 6075-6079, DOI: https://doi.org/10.1016/j.jeurceramsoc.2021.05.041.
- (10) Ye, R. J.; Tsai, C. L.; Ihrig, M.; Sevinc, S.; Rosen, M.; Dashjav, E.; Sohn, Y. J.; Figgemeier, E.; Finsterbusch, M. Water-Based Fabrication of Garnet-Based Solid Electrolyte Separators for Solid-State Lithium Batteries. *Green Chem.* **2020**, *22* (15), 4952-4961, DOI: 10.1039/d0gc01009j.
- (11) Kim, K. J.; Rupp, J. L. M. All Ceramic Cathode Composite Design and Manufacturing Towards Low Interfacial Resistance for Garnet-based Solid-state Lithium Batteries. *Energy Environ. Sci.* **2020**, *13* (12), 4930-4945. DOI: 10.1039/D0EE02062A.
- (12) Xiao, Y.; Miara, L. J.; Wang, Y.; Ceder, G. Computational Screening of Cathode Coatings for Solid-State Batteries. *Joule* **2019**, *3* (5), 1252-1275. DOI: 10.1016/j.joule.2019.02.006.

- (13) Famprikis, T.; Canepa, P.; Dawson, J. A.; Islam, M. S.; Masquelier, C. Fundamentals of Inorganic Solid-State Electrolytes for Batteries. *Nat. Mater.* **2019**, *18* (12), 1278-1291. DOI: 10.1038/s41563-019-0431-3.
- (14) Ihrig, M.; Ye, R.; Laptev, A. M.; Grüner, D.; Guerdelli, R.; Scheld, W. S.; Finsterbusch, M.; Wiemhöfer, H.-D.; Fattakhova-Rohlfing, D.; Guillon, O. Polymer–Ceramic Composite Cathode with Enhanced Storage Capacity Manufactured by Field-Assisted Sintering and Infiltration. *ACS Appl. Energy Mater.* **2021**, 4 (10), 10428-10432. DOI: 10.1021/acsaem.1c02667.
- (15) Ye, R.; Ihrig, M.; Imanishi, N.; Finsterbusch, M.; Figgemeier, E. A Review on Li(+)/H(+) Exchange in Garnet Solid Electrolytes: From Instability against Humidity to Sustainable Processing in Water. *ChemSusChem* **2021**, *14* (20), 4397-4407, DOI: 10.1002/cssc.202101178.
- (16) Gao, Y.; Nolan, A. M.; Du, P.; Wu, Y.; Yang, C.; Chen, Q.; Mo, Y.; Bo, S.-H. Classical and Emerging Characterization Techniques for Investigation of Ion Transport Mechanisms in Crystalline Fast Ionic Conductors. *Chem. Rev.* **2020**, *120* (13), 5954-6008. DOI: 10.1021/acs.chemrev.9b00747.
- (17) Banerjee, A.; Wang, X.; Fang, C.; Wu, E. A.; Meng, Y. S. Interfaces and Interphases in All-Solid-State Batteries with Inorganic Solid Electrolytes. *Chem. Rev.* **2020**, *120* (14), 6878-6933. DOI: 10.1021/acs.chemrev.0c00101.
- (18) Ohta, S.; Kobayashi, T.; Asaoka, T. High Lithium Ionic Conductivity in the Garnet-Type Oxide Li_{7-x}La₃(Zr_{2-x}, Nb_x)O₁₂ (x=0-2). *J. Power Sources* **2011**, *196* (6), 3342-3345. DOI: 10.1016/j.jpowsour.2010.11.089.

- (19) Liu, T.; Ren, Y.; Shen, Y.; Zhao, S.-X.; Lin, Y.; Nan, C.-W. Achieving High Capacity in Bulk-Type Solid-State Lithium Ion Battery Based on Li_{6.75}La₃Zr_{1.75}Ta_{0.25}O₁₂ Electrolyte: Interfacial Resistance. *J. Power Sources* **2016**, *324*, 349-357. DOI: 10.1016/j.jpowsour.2016.05.111.
- (20) Yamada, H.; Ito, T.; Hongahally Basappa, R.; Bekarevich, R.; Mitsuishi, K. Influence of Strain on Local Structure and Lithium Ionic Conduction in Garnet-Type Solid Electrolyte. *J. Power Sources* **2017**, *368*, 97-106. DOI: 10.1016/j.jpowsour.2017.09.076.
- (21) Ohta, S.; Seki, J.; Yagi, Y.; Kihira, Y.; Tani, T.; Asaoka, T. Co-sinterable Lithium Garnet-type Oxide Electrolyte with Cathode for All-Solid-State Lithium Ion Battery. *J. Power Sources* **2014**, *265*, 40-44. DOI: 10.1016/j.jpowsour.2014.04.065.
- (22) Park, K.; Yu, B.-C.; Jung, J.-W.; Li, Y.; Zhou, W.; Gao, H.; Son, S.; Goodenough, J. B. Electrochemical Nature of the Cathode Interface for a Solid-State Lithium-Ion Battery: Interface between LiCoO₂ and Garnet-Li₇La₃Zr₂O₁₂. *Chem. Mater.* **2016**, *28* (21), 8051-8059. DOI: 10.1021/acs.chemmater.6b03870.
- (23) Kim, K. H.; Iriyama, Y.; Yamamoto, K.; Kumazaki, S.; Asaka, T.; Tanabe, K.; Fisher, C. A. J.; Hirayama, T.; Murugan, R.; Ogumi, Z. Characterization of the Interface between LiCoO₂ and Li₇La₃Zr₂O₁₂ in an All-Solid-State Rechargeable Lithium Battery. *J. Power Sources* **2011**, *196* (2), 764-767. DOI: 10.1016/j.jpowsour.2010.07.073.
- (24) Laptev, A. M.; Zheng, H.; Bram, M.; Finsterbusch, M.; Guillon, O. High-Pressure Field Assisted Sintering of Half-Cell for All-Solid-State Battery. *Mater. Lett.* **2019**, *247*, 155-158. DOI: 10.1016/j.matlet.2019.03.109.

- (25) Ihrig, M.; Finsterbusch, M.; Tsai, C.-L.; Laptev, A. M.; Tu, C.-h.; Bram, M.; Sohn, Y. J.; Ye, R.; Sevinc, S.; Lin, S.-k.; Fattakhova-Rohlfing, D.; Guillon, O. Low Temperature Sintering of Fully Inorganic All-Solid-State Batteries Impact of Interfaces on Full Cell Performance. *J. Power Sources* **2021**, *482*, No 228905. DOI: 10.1016/j.jpowsour.2020.228905.
- (26) Tsai, C.-L.; Ma, Q.; Dellen, C.; Lobe, S.; Vondahlen, F.; Windmüller, A.; Grüner, D.; Zheng, H.; Uhlenbruck, S.; Finsterbusch, M.; Tietz, F.; Fattakhova-Rohlfing, D.; Buchkremer, H. P.; Guillon, O. A Garnet Structure-Based All-Solid-State Li Battery without Interface Modification: Resolving Incompatibility Issues on Positive Electrodes. *Sustain. Energy Fuels* **2019**, (1), 280-291. DOI: 10.1039/C8SE00436F.
- (27) Ohta, S.; Kobayashi, T.; Seki, J.; Asaoka, T. Electrochemical Performance of an All-Solid-State Lithium Ion Battery with Garnet-Type Oxide Electrolyte. *J. Power Sources* **2012**, *202*, 332-335. DOI: 10.1016/j.jpowsour.2011.10.064.
- (28) Han, F.; Zhu, Y.; He, X.; Mo, Y.; Wang, C. Electrochemical Stability of Li₁₀GeP₂S₁₂ and Li'La₃Zr₂O₁₂ Solid Electrolytes. *Adv. Energy Mater.* **2016**, *6* (8), No 1501590. DOI: 10.1002/aenm.201501590.
- (29) Koerver, R.; Zhang, W.; de Biasi, L.; Schweidler, S.; Kondrakov, A. O.; Kolling, S.; Brezesinski, T.; Hartmann, P.; Zeier, W. G.; Janek, J. Chemo-Mechanical Expansion of Lithium Electrode Materials on the Route to Mechanically Optimized All-Solid-State Batteries. *Energy Environ. Sci.* **2018**, *11* (8), 2142-2158. DOI: 10.1039/C8EE00907D.
- (30) Bendersky, L.; Tan, H.; Bharathi Karuppanan, K.; Li, Z.-P.; Johnston-Peck, A. Crystallography and Growth of Epitaxial Oxide Films for Fundamental Studies of Cathode

Materials Used in Advanced Li-Ion Batteries. *Crystals* **2017**, 7 (5), No 127. DOI: 10.3390/cryst7050127.

- (31) Junji, A.; Akira, T.; Kunimitsu, K.; Norihito, K.; Yasushi, I.; Junji, A. Crystal Structure of Fast Lithium-Ion-Conducting Cubic Li₇La₃Zr₂O₁₂. *Chem. Lett.* **2011**, *40* (1), 60-62. DOI: 10.1246/cl.2011.60.
- (32) Panahian Jand, S.; Kaghazchi, P. Theoretical Study of Cubic-Li₇La₃Zr₂O₁₂(001)/LiCoO₂(10–14) Interface. *MRS Commun.* **2018**, *8* (2), 591-596. DOI: 10.1557/mrc.2018.33.
- (33) Zhang, N.; Long, X.; Wang, Z.; Yu, P.; Han, F.; Fu, J.; Ren, G.; Wu, Y.; Zheng, S.; Huang, W.; Wang, C.; Li, H.; Liu, X. Mechanism Study on the Interfacial Stability of a Lithium Garnet-Type Oxide Electrolyte against Cathode Materials. *ACS Appl. Energy Mater.* **2018**, *1* (11), 5968-5976. DOI: 10.1021/acsaem.8b01035.
- (34) Jalem, R.; Morishita, Y.; Okajima, T.; Takeda, H.; Kondo, Y.; Nakayama, M.; Kasuga, T. Experimental and First-Principles DFT Study on the Electrochemical Reactivity of Garnet-Type Solid Electrolytes with Carbon. *J. Mater. Chem. A* **2016**, *4* (37), 14371-14379. DOI: 10.1039/C6TA04280E.
- (35) Wang, Z.; Santhanagopalan, D.; Zhang, W.; Wang, F.; Xin, H. L.; He, K.; Li, J.; Dudney, N.; Meng, Y. S. In Situ STEM-EELS Observation of Nanoscale Interfacial Phenomena in All-Solid-State Batteries. *Nano Lett.* **2016**, *16* (6), 3760-3767. DOI: 10.1021/acs.nanolett.6b01119.
- (36) Wang, Z.; Lee, J. Z.; Xin, H. L.; Han, L.; Grillon, N.; Guy-Bouyssou, D.; Bouyssou, E.; Proust, M.; Meng, Y. S. Effects of Cathode Electrolyte Interfacial (CEI) Layer on Long Term

- Cycling of All-Solid-State Thin-Film Batteries. *J. Power Sources* **2016**, *324*, 342-348. DOI: 10.1016/j.jpowsour.2016.05.098.
- (37) Julien, C. M.; Mauger, A.; Hussain, O. M. Sputtered LiCoO₂ Cathode Materials for All-Solid-State Thin-film Lithium Microbatteries. *Materials* **2019**, *12* (17), No 2687. DOI: 10.3390/ma12172687.
- (38) Otoyama, M.; Ito, Y.; Hayashi, A.; Tatsumisago, M. Raman Imaging for LiCoO₂ Composite Positive Electrodes in All-Solid-State Lithium Batteries Using Li₂S–P₂S₅ Solid Electrolytes. *J. Power Sources* **2016**, *302*, 419-425. DOI: 10.1016/j.jpowsour.2015.10.040.
- (39) Miara, L.; Windmuller, A.; Tsai, C. L.; Richards, W. D.; Ma, Q. L.; Uhlenbruck, S.; Guillon, O.; Ceder, G. About the Compatibility between High Voltage Spinel Cathode Materials and Solid Oxide Electrolytes as a Function of Temperature. *ACS Appl. Mater. Interfaces* **2016**, *8* (40), 26842-26850. DOI: 10.1021/acsami.6b09059.
- (40) Zhu, Y.; He, X.; Mo, Y. First Principles Study on Electrochemical and Chemical Stability of Solid Electrolyte–Electrode Interfaces in All-Solid-State Li-Ion Batteries. *J. Mater. Chem. A* **2016**, *4* (9), 3253-3266. DOI: 10.1039/C5TA08574H.
- (41) Tsai, C. L.; Roddatis, V.; Chandran, C. V.; Ma, Q.; Uhlenbruck, S.; Bram, M.; Heitjans, P.; Guillon, O. Li₇La₃Zr₂O₁₂ Interface Modification for Li Dendrite Prevention. *ACS Appl. Mater. Interfaces* **2016**, *8* (16), 10617-10626. DOI: 10.1021/acsami.6b00831.
- (42) Santhosha, A. L.; Medenbach, L.; Buchheim, J. R.; Adelhelm, P. The Indium–Lithium Electrode in Solid-State Lithium-Ion Batteries: Phase Formation, Redox Potentials, and Interface Stability. *Batter. Supercaps* **2019**, *2* (6), 524-529. DOI: 10.1002/batt.201800149.

- (43) Kresse, G.; Joubert, D. From Ultrasoft Pseudopotentials to the Projector Augmented-Wave Method. *Phys. Rev. B* **1999**, *59* (3), 1758-1775. DOI: 10.1103/PhysRevB.59.1758.
- (44) Blöchl, P. E. Projector Augmented-Wave Method. *Phys. Rev. B* **1994**, *50* (24), 17953-17979. DOI: 10.1103/PhysRevB.50.17953.
- (45) Perdew, J. P.; Burke, K.; Ernzerhof, M. Generalized Gradient Approximation Made Simple. *Phys. Rev. Lett.* **1996,** 77 (18), 3865-3868. DOI: 10.1103/PhysRevLett.77.3865.
- (46) Jain, A.; Hautier, G.; Ong, S. P.; Moore, C. J.; Fischer, C. C.; Persson, K. A.; Ceder, G. Formation enthalpies by mixing GGA and GGA + U calculations. *Phys. Rev. B* **2011**, *84* (4), No 045115. DOI: 10.1103/PhysRevB.84.045115.
- (47) Bram, M.; Laptev, A.; Prasad Mishra, T.; Nur, K.; Kindelmann, M.; Ihrig, M.; Pereira da Silva, J.; Steinert, R.; Buchkremer, H.-P.; Litnovsky, A.; Klein, F.; Gonzalez-Julian, J.; Guillon, O. Application of Electric Current Assisted Sintering Techniques for the Processing of Advanced Materials. *Adv. Eng. Mater.* 22 (6), No. 2000051. DOI: 10.1002/adem.202000051.
- (48) Finsterbusch, M.; Danner, T.; Tsai, C.-L.; Uhlenbruck, S.; Latz, A.; Guillon, O. High Capacity Garnet-Based All-Solid-State Lithium Batteries: Fabrication and 3D-Microstructure Resolved Modeling. *ACS Appl. Mater. Interfaces* **2018**, *10* (26), 22329-22339. DOI: 10.1021/acsami.8b06705.
- (49) Mücke, R.; Finsterbusch, M.; Kaghazchi, P.; Fattakhova-Rohlfing, D.; Guillon, O. Modelling Electro-Chemical Induced Stresses in All-Solid-State Batteries: Anisotropy Effects in Cathodes and Cell Design Optimisation. *J. Power Sources* **2021**, *489*, No 229430. DOI: 10.1016/j.jpowsour.2020.229430.

- (50) Kotobuki, M.; Kanamura, K.; Sato, Y.; Yoshida, T. Fabrication of All-Solid-State Lithium Battery with Lithium Metal Anode Using Al₂O₃-Added Li₇La₃Zr₂O₁₂ Solid Electrolyte. *J. Power Sources* **2011**, *196* (18), 7750-7754. DOI: 10.1016/j.jpowsour.2011.04.047.
- (51) Song, K. Y.; Jang, G. S.; Tao, J.; Lee, J. H.; Joo, S. K. Effects of Electrode Thickness on Three-Dimensional NiCrAl Metal Foam Cathode for Lithium Ion Battery. *J. Nanosci. Nanotechnol.* **2018**, *18* (2), 992-998. DOI: 10.1166/jnn.2018.13953.
- (52) Ren, Y.; Liu, T.; Shen, Y.; Lin, Y.; Nan, C.-W. Chemical Compatibility between Garnet-Like Solid State Electrolyte Li_{6.75}La₃Zr_{1.75}Ta_{0.25}O₁₂ and Major Commercial Lithium Battery Cathode Materials. *J. Materiomics* **2016**, *2* (3), 256-264. DOI: 10.1016/j.jmat.2016.04.003.
- (53) Zhu, Y.; He, X.; Mo, Y. Origin of Outstanding Stability in the Lithium Solid Electrolyte Materials: Insights from Thermodynamic Analyses Based on First-Principles Calculations. *ACS Appl. Mater. Interfaces* **2015**, *7* (42), 23685-23693. DOI: 10.1021/acsami.5b07517.
- (54) Liu, T.; Zhang, Y.; Chen, R.; Zhao, S.-X.; Lin, Y.; Nan, C.-W.; Shen, Y. Non-Successive Degradation in Bulk-Type All-Solid-State Lithium Battery with Rigid Interfacial Contact. *Electrochem. Commun.* **2017**, *79*, 1-4. DOI: 10.1016/j.elecom.2017.03.016.
- (55) Koerver, R.; Aygün, I.; Leichtweiß, T.; Dietrich, C.; Zhang, W.; Binder, J. O.; Hartmann, P.; Zeier, W. G.; Janek, J. Capacity Fade in Solid-State Batteries: Interphase Formation and Chemomechanical Processes in Nickel-Rich Layered Oxide Cathodes and Lithium Thiophosphate Solid Electrolytes. *Chem. Mater.* **2017**, *29* (13), 5574-5582. DOI: 10.1021/acs.chemmater.7b00931.

- (56) Okumura, T.; Takeuchi, T.; Kobayashi, H. All-Solid-State Lithium-Ion Battery Using Li_{2.2}C_{0.8}B_{0.2}O₃ Electrolyte. *Solid State Ion.* **2016**, *288*, 248-252. DOI: 10.1016/j.ssi.2016.01.045.
- (57) Nasir Khan, M.; Bashir, J. Synthesis and Structural Refinement of LiAl_xCo_{1-x}O₂ system. *Mater. Res. Bull.* **2006**, *41* (9), 1589-1595. DOI: 10.1016/j.materresbull.2006.02.032.
- (58) Huang, B.; Zhao, Z.; Sun, Y.; Wang, M.; Chen, L.; Gu, Y. Lithium-Ion Conductor LiAlO₂ coated LiNi_{0.8}Mn_{0.1}Co_{0.1}O₂ as cathode material for lithium-ion batteries. *Solid State Ion.* **2019**, *338*, 31-38. DOI: 10.1016/j.ssi.2019.05.005.
- (59) Cao, H.; Xia, B.; Zhang, Y.; Xu, N. LiAlO₂-Coated LiCoO₂ as Cathode Material for Lithium Ion Batteries. *Solid State Ion.* **2005**, *176* (9), 911-914. DOI: 10.1016/j.ssi.2004.12.001.
- (60) Miara, L. J.; Richards, W. D.; Wang, Y. E.; Ceder, G. First-Principles Studies on Cation Dopants and Electrolyte|Cathode Interphases for Lithium Garnets. *Chem. Mater.* **2015**, *27* (11), 4040-4047. DOI: 10.1021/acs.chemmater.5b01023.
- (61) Tian, H.-K.; Chakraborty, A.; Talin, A. A.; Eisenlohr, P.; Qi, Y. Evaluation of The Electrochemo-Mechanically Induced Stress in All-Solid-State Li-Ion Batteries. *J. Electrochem. Soc.* **2020**, *167* (9), No 090541. DOI: 10.1149/1945-7111/ab8f5b.
- (62) Wang, P.; Qu, W.; Song, W.-L.; Chen, H.; Chen, R.; Fang, D. Electro-Chemo-Mechanical Issues at the Interfaces in Solid-State Lithium Metal Batteries. *Adv. Funct. Mater.* **2019**, *29* (27), No 1900950. DOI: 10.1002/adfm.201900950.
- (63) Vardar, G.; Bowman, W. J.; Lu, Q.; Wang, J.; Chater, R. J.; Aguadero, A.; Seibert, R.; Terry, J.; Hunt, A.; Waluyo, I.; Fong, D. D.; Jarry, A.; Crumlin, E. J.; Hellstrom, S. L.; Chiang, Y.-M.; Yildiz, B. Structure, Chemistry, and Charge Transfer Resistance of the Interface between

- Li₇La₃Zr₂O₁₂ Electrolyte and LiCoO₂ Cathode. *Chem. Mater.* **2018**, *30* (18), 6259-6276. DOI: 10.1021/acs.chemmater.8b01713.
- (64) Kaewmala, S.; Limphirat, W.; Yordsri, V.; Kim, H.; Muhammad, S.; Yoon, W.-S.; Srilomsak, S.; Limthongkul, P.; Meethong, N. Structural and Electrochemical Kinetic Properties of 0.5Li₂MnO₃·0.5LiCoO₂ Cathode Materials with Different Li₂MnO₃ Domain Sizes. *Sci. Rep.* **2019**, *9* (1), No 427. DOI: 10.1038/s41598-018-36593-9.
- (65) Bianchini, M.; Wang, J.; Clément, R. J.; Ouyang, B.; Xiao, P.; Kitchaev, D.; Shi, T.; Zhang, Y.; Wang, Y.; Kim, H.; Zhang, M.; Bai, J.; Wang, F.; Sun, W.; Ceder, G. The Interplay between Thermodynamics and Kinetics in the Solid-State Synthesis of Layered Oxides. *Nat. Mater.* **2020**, *19* (10), 1088-1095. DOI: 10.1038/s41563-020-0688-6.
- (66) Tadanaga, K.; Takano, R.; Ichinose, T.; Mori, S.; Hayashi, A.; Tatsumisago, M. Low Temperature Synthesis of Highly Ion Conductive Li₇La₃Zr₂O₁₂–Li₃BO₃ Composites. *Electrochem. Commun.* **2013**, *33*, 51-54. DOI: 10.1016/j.elecom.2013.04.004.
- (67) Özer, N.; Lampert, C. M. Electrochemical Lithium Insertion in Sol-Gel Deposited LiNbO₃ Films. *Sol. Energy Mater. Sol. Cells* **1995**, *39* (2-4), 367-375. DOI: 10.1016/0927-0248(96)80002-X.

Graphical Abstract:

